The translaminar fracture toughness of high-performance polymer fibre composites and their carbon fibre hybrids

Yoran Geboes[*1,2], Amalia Katalagarianakis[1], Jeroen Soete[1], Jan Ivens[1], Yentl Swolfs[1]

[1]Department of Materials Engineering, KU Leuven, Kasteelpark Arenberg 44 box 2450, Belgium
[2]SIM vzw, Technologiepark 48, BE-9052 Zwijnaarde, Belgium

Abstract

The translaminar fracture toughness is a key property that governs the damage tolerance and notch sensitivity of fibre-reinforced composites. Compact tension tests were performed to investigate the translaminar fracture toughness of composites reinforced with three types of high-performance polymer fibres: polyarylate (PAR), polybenzobisoxazole (PBO) and aramid fibre. A carbon fibre composite was used as the reference system. The propagation translaminar fracture toughnesses of the PAR and PBO fibre composites were 492 kJ/m² and 547 kJ/m², respectively. These are among the highest translaminar fracture toughness values recorded in the literature. It was hypothesized that the fibrillation of the fibres upon failure was an important energy dissipating mechanism alongside pull-outs that were much longer than for carbon fibre. Replacing a small strip of a carbon fibre ply by a strip of PAR or PBO fibres successfully reinforced the material by locally arresting crack growth. By contrast, the performance of the aramid fibre composites and their hybrids with carbon fibre was lacklustre. The results presented in this work can be used to further improve the safety of composite parts by optimising the design for damage tolerance while also reducing the weight of the parts.

Key words: A. Hybrid composites; A. Polymer fibres; B. Fracture toughness; D. Fractography; Compact tension

1. Introduction

The potential weight savings in failure-sensitive applications that can be made by using carbon fibre (CF) reinforced polymer composites is currently limited. The failure

[*] Corresponding author: Y. Geboes (yoran.geboes@kuleuven.be), Tel: +32 16 37 33 86

behaviour of fibre-reinforced composites is not fully understood yet, which leads to overdimensioned parts. Hence, the parts are heavier and more expensive than strictly required. The fracture behaviour of laminated composites can be split into three types. The intralaminar and interlaminar fracture, where the crack propagates parallel to the fibre direction, have been examined extensively [1-8]. The interest in translaminar fracture toughness increased in just the last 15 years despite being an important failure-related property as it governs the damage tolerance and notch sensitivity of a fibre-reinforced composite. The translaminar fracture toughness is the fracture toughness associated with a crack propagating perpendicular to the fibre direction, thus fracturing the fibres. In conventional brittle fibre composites, such as carbon and glass fibre composites, the main energy dissipating mechanisms are fibre-matrix debonding and fibre pull-out [9-18].

A promising strategy to increase the translaminar fracture toughness of CF composites is by introducing fibre types that possess additional energy dissipating mechanisms. One of those promising fibre types are high-performance polymer fibres (HPPFs). These fibres fibrillate upon failure due to the extreme anisotropy [19] and their fibrillar structure [20-22]. This fibrillation creates a lot of new surface area, which dissipates energy. Herráez et al. [23] reported a fracture energy of 1101 J/m² for Kevlar KM2 aramid fibres. This is significantly higher than the 4 – 52 J/m² reported in the literature for carbon and glass fibres [23, 24].

However, currently only limited research has been documented on the potential of HPPFs to obtain composites with a high translaminar fracture toughness. Syed Abdullah et al. [25] investigated the translaminar fracture toughness of PAR fibres using a novel compact tension specimen geometry, showing promising results with an initiation toughness of 130 – 145 kJ/m² and a propagation toughness of 250 – 260 kJ/m². This is at the higher end of the typical values recorded in the literature for CF composites,

which are in the 20 – 150 kJ/m² range for initiation and 20 – 280 kJ/m² range for propagation [10, 26-29]. As only one type of HPPF was examined, no direct link of the measured results to a particular fibre property could be made.

Another promising strategy to create materials with a high fracture resistance originates in nature. Using a bioinspired design, Kolednik et al. [30] concluded that a much higher fracture resistance can be obtained by incorporating compliant layers without strongly reducing the stiffness of the structure. Sistaninia and Kolednik [31] examined the influence of a strip of softer material in a layer with identical elastic properties. The crack driving force was found to be greatly reduced at the soft-to-hard transition. Therefore, it was deemed the critical position for possible crack arrest. In a follow-up investigation, Sistaninia and Kolednik [32] determined the optimal width of the strip and the optimal strip-to-ply yield stress ratio. Also, the optimal spacing between multiple strips in a ply was studied. Inspired by the work of Kolednik, Swolfs and Pinho [33] combined two fibre types into a single laminate, called fibre-hybridisation, to increase the translaminar fracture toughness. Toughness improvements of 20 – 60 % were found by embedding a strip of CF in a glass fibre ply.

Several studies have examined the translaminar fracture of fibre-hybrid composites [33-39]. As a continuation of the work of Amacher et al. [37], Cugnoni et al. [38] examined three types of quasi-isotropic thin-ply hybrid composites: two types of carbon/carbon ply-by-ply hybrids (0°/0° and 0°/90°) and an aramid fibre tows in CF plies hybrid. The reference and hybrid laminates showed a comparable initiation toughness, but all the hybrids displayed an improved crack resistance with increasing crack growth. The carbon/carbon hybrids showed an improvement in propagation toughness up to 18%. This improvement was explained by an increase in fibre bundle pull-out lengths due to controlled fibre fragmentation, and also the promotion of a larger process zone in the 0°/90° hybrid. No exact propagation toughness value could be determined for the

carbon/aramid hybrid due to premature compressive failure. Extension of the aramid fibres further away from the fracture surface was observed, suggesting that the aramid fibres continue to bridge the crack at larger openings, but further research was required to verify that hypothesis.

Katafiasz et al. [39] investigated the mode I laminate toughness of carbon/S-glass interply hybrids and carbon/PAR intraply hybrids using the same novel compact tension specimen geometry as Syed Abdullah et al. [25]. The carbon/S-glass interply hybrids displayed an R-curve in between its non-hybrid carbon and S-glass fibre reinforced reference systems, indicating that the mixing theory might be applicable to predict the behaviour of interply fibre hybrids. The carbon/PAR intraply hybrid showed promising results with a measured fracture toughness higher than the other material systems investigated in the paper. A direct correlation of the fibre pull-out lengths with the measured laminate/translaminar fracture toughness was observed. However, making a direct comparison in the recorded toughness values is not easy due to the differences in ply thickness and fibre architecture of the different materials systems used.

This paper therefore examines the translaminar fracture toughness of composites reinforced with three types of HPPFs to better understand the potential of HPPFs to obtain composites with a good damage tolerance and notch sensitivity. CF composites were used as the reference system and to examine the performance of high-performance polymer/carbon hybrids. To successfully characterise the translaminar fracture toughness of the different samples, a special stacking sequence was utilised. This paper also presents the first direct translaminar fracture toughness comparison between composites reinforced with different types of HPPFs. Furthermore, the potential of HPPFs to locally arrest the crack by incorporating a strip of HPPF in a CF ply is investigated for the first time.

2. Materials and methods

2.1 Materials

Three types of high-performance polymer fibres were investigated: PAR (polyarylate, brand name Vectran), PBO (polybenzobisoxazole, brand name Zylon) and aramid (brand name Twaron) fibres. A conventional T300 CF served as the reference fibre. Table I presents the fibre properties. Composites were manufactured using the fibres by in-house prepreg production on a Research Tool Corporation Model 30 drumwinder. A two-component epoxy system suitable for prepreg production was used to produce the composites. Table II summarises the properties that were characterised in-house.

Table I: Properties of the fibres used in this research. The properties of the HPPFs are generic properties supplied by its manufacturer, whereas the CF data is batch specific. The properties with an asterisk are calculated from the supplied properties.

		PAR	**PBO**	**Aramid**	**CF**
Manufacturer		Kuraray	Toyobo	Teijin	Toray
Fibre		Vectran HT	Zylon HM	Twaron 2200	T300 40B
Fibre diameter*	[µm]	22.5	11.6	11.9	6.9
Tensile strength	[MPa]	3200	5800	3100	3800
Tensile modulus	[GPa]	75	270	110	231
Elongation at break	[%]	3.8	2.5	2.7	1.64
Density	[g/cm³]	1.41	1.56	1.45	1.76
Tow size	[#]	300	996	1000	3000
Yarn linear density	[dtex]	1670	1640	1610	2000
Yarn cross-sectional area*	[mm²]	0.119	0.105	0.111	0.114

Table II: Properties of the matrix used in this research. The properties were measured in-house [40]. The properties with an asterisk were measured at an average strain rate of 9e-5 s^{-1}.

Manufacturer	**Sicomin**	
Type	**SiPreg SR8500/KTA313**	
Yield strength*	[MPa]	103
Tensile modulus*	[GPa]	3.6
Poisson's ratio*	[/]	0.42
Density	[g/cm³]	1.17

2.2 Manufacturing

Following the manufacturer's guidelines, 21 grams of hardener was used per 100 grams of resin. Prior to the impregnation process, the mixed epoxy system was degassed for 15 minutes in a vacuum oven to minimise porosity in the cured composites.

25 prepreg plies of 300x300mm² were stacked to obtain 6-9 mm thick panels. A roller was used to remove entrapped air after adding each layer. The prepreg plates were cured in an autoclave for 4 hours at 60°C and post-cured in the autoclave for 2 hours at 120°C, following the guidelines of the manufacturer of the epoxy system. The layup was under a vacuum pressure of -0.8 bar. An overpressure of 3 bar was exerted by pressurising the autoclave with nitrogen. After curing, the quality of the manufactured plates was checked using optical microscopy, confirming a good impregnation quality. The light microscopy pictures were also used to determine the fibre volume fraction via thresholding. The pictures were first converted to greyscale pictures. Next, a threshold was set manually to categorise the pixels between pixels corresponding to the matrix and pixels corresponding to the fibres. The fibre volume fraction was then calculated as the number of fibre-pixels to the total number of pixels. To assess the sensitivity of the result to the manual selection of the threshold, the results obtained using thresholding were compared to fibre volume fraction determination through matrix digestion using piranha solution, following the ASTM D3171 standard. Both techniques showed similar results. Optical microscopy was also used to measure the thickness of the plies.

2.3 Compact tension tests

2.3.1 Specimen design and preparation

The specimen design was based on the doubly-tapered compact tension geometry of Blanco et al. [41], shown in Figure 1. The outer geometry and part of the notch were waterjet cut. The cuts were initiated at least two cm away from the samples to avoid damage in the samples introduced during the start of a cut. The notch obtained after water jetting was sharpened using a slitting saw that had sharp teeth with a tip angle of

20°. The notch was further sharpened with a razorblade to obtain a notch with a 50 µm radius tip, which is vital to obtain the correct initiation toughness [13]. The two holes in the sample were drilled using a composite twist drill bit specifically designed for composite materials. This way, high-quality holes without delaminations or damage at the holes were acquired.

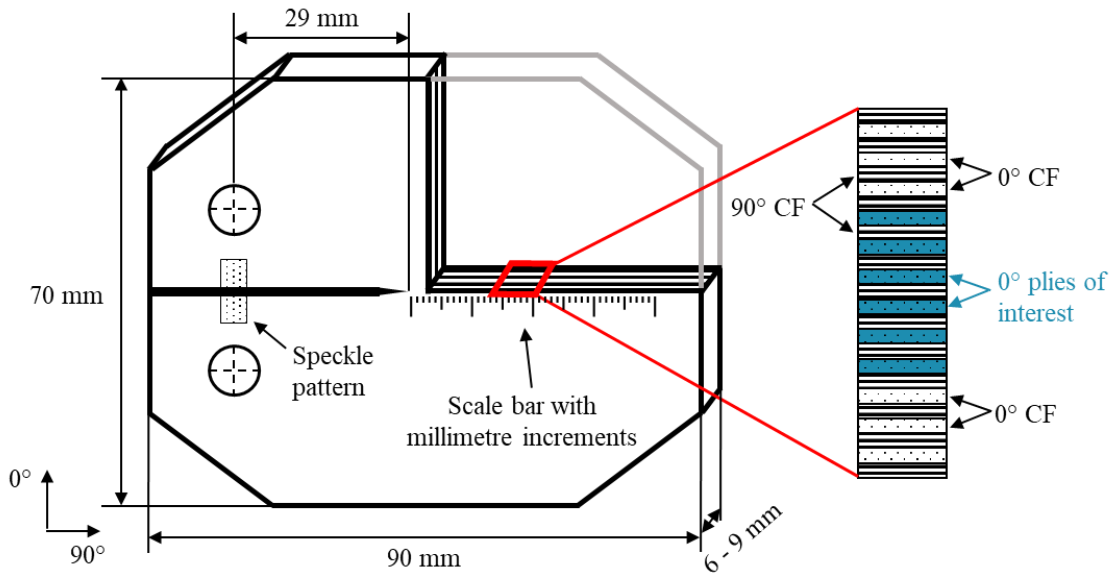

Figure 1: The design of the compact tension test samples based on the doubly-tapered test geometry. For more details on the geometry, the reader is referred to the paper of Blanco et al [41]. The stacking sequence of the samples is also shown. Only the middle six 0° plies varied in content, the other 19 plies were always made of CF plies in all the samples.

The occurrence of undesired failure mechanisms during testing, such as compressive failure and buckling, is quite common with compact tension specimens. This led to the development of optimised specimen geometries, such as the doubly-tapered compact tension geometry of Blanco et al. [41], which we have used in this research, and the curved compact tension geometry of Syed Abdullah et al. [25] and Katafiasz et al. [39]. As high-performance polymer fibres have notoriously poor compressive properties [42], this made the issues even more prevalent. Problems were encountered when testing non-hybrid composites reinforced with the high-performance polymer fibres. Even when using geometries containing an edge groove, which is similar in philosophy to the through-the-thickness groove used by Abdullah et al. [25] and Katafiasz et al. [39],

difficulties were met. However, the stacking sequence presented in Figure 1 was successful in preventing undesired failure mechanisms during testing. Moreover, the specimen design was less tedious to prepare and easier in terms of data processing compared to the strategy used by Abdullah et al. [25] and Katafiasz et al. [39].

An alternating 0°/90° ply stacking sequence was used to prevent ply blocking effects [43]. Only the middle six 0° plies were made with the fibres of interest to characterize the performance of composites reinforced with those fibres. In all lay-up designs, the three outermost 0° plies on each side consisted of CFs. This prevented undesired failure mechanisms during testing, such as compressive failure and buckling. The 90° plies consisted of CFs in all lay-up designs. The 90° CF plies were used to prevent undesired failure mechanisms during testing and to help guide the crack in a single plane.

The measured critical strain energy release rate $G_{Ic}^{measured}$ will be a combination of the translaminar fracture toughness contribution of the 0° plies $G_{Ic}^{0^\circ}$ and the intralaminar fracture toughness contribution of the 90° plies $G_{Ic}^{90^\circ}$, see equation 1. t_{0°, t_{90° and t_{lam} are the thickness of the 0° plies, the thickness of the 90° plies and the total thickness of the laminate respectively.

$$G_{Ic}^{measured} = \frac{t_{0^\circ}}{t_{lam}} G_{Ic}^{0^\circ} + \frac{t_{90^\circ}}{t_{lam}} G_{Ic}^{90^\circ} \quad (1)$$

However, from the literature it is known that the translaminar fracture toughness of CF composites is around three orders of magnitude higher than its intralaminar fracture toughness [7]. The contribution of the 90° plies to the measured result can hence be neglected [44, 45].The experimentally measured toughness can therefore be considered as a contribution of just the 0° plies, see equation 2.

$$G_{Ic}^{measured} = \frac{t_{0^\circ\, interest}}{t_{0^\circ\, total}} G_{Ic}^{0^\circ\, interest} + \frac{t_{0^\circ\, CF}}{t_{0^\circ\, total}} G_{Ic}^{0^\circ\, CF} \quad (2)$$

Ortega et al. [46] investigated the ability to use the mixing theory on interply hybrids and concluded that the mixing theory was able to roughly predict the toughness of the hybrid laminates. A similar observation was made by Katafiasz et al. [39]. The translaminar fracture toughness of only the plies of interest $G_{Ic}^{0^\circ\,\mathrm{interest}}$ can then be calculated by removing the contribution of the 0° CF plies $G_{Ic}^{0^\circ\,\mathrm{CF}}$. The thickness of the 0° plies of interest $t_{0^\circ\,\mathrm{interest}}$ and the thickness of the 0° CF plies $t_{0^\circ\,\mathrm{CF}}$ have to be taken into account. $t_{0^\circ\,\mathrm{total}}$ is the total thickness of the 0° plies. This contribution of the 0° CF plies was calculated by first characterising the translaminar fracture toughness of these plies in samples with the plies of interest also being CF plies. The ply thickness was measured using optical microscopy.

Different design strategies were examined: lay-ups with full plies of one of the fibre types were examined to characterize that fibre's base behaviour. These samples will be referred to as "ply samples". So-called "strip samples" were tested to inspect the crack arresting capabilities of the different fibre types, and to study the effect of the transition between a more and a less compliant material. Figure 2 shows a schematic illustration of a strip sample. In the strip samples, a six mm wide strip was removed in CF plies and replaced by a 6 mm wide strip of HPPFs. However, some spreading and moving of the strips during curing was noticed due to resin bleed out during curing. This caused the strips to be slightly wider than the intended width of six mm. Moreover, the moving of the strips caused them not to be in the same location over the different plies. Therefore, the crack tip did not encounter the reinforcing strip material in all the plies-of-interest at once upon entering the strip region. This decreased the effect of the transition between a more and a less compliant material, which complicated quantifying the influence of the strips. A full overview of the manufactured lay-up designs examined can be found in Table III.

Although ideally all the plies were the same for all materials, variations in thickness were unavoidable in the in-house produced prepregs. Therefore, eight instead of six plies of interest were used for the aramid ply samples due to the lower ply thickness compared to the other HPPF types. Having a comparable total thickness of the aramid fibre ply samples to the PAR and PBO fibre ply specimens was important to improve the resistance of the samples to buckling. Moreover, in this way a possible influence of having a different total sample thickness was avoided [45, 47]. No influence on the measurements is expected by having more aramid fibre plies as they were separated by a 90° ply [43].

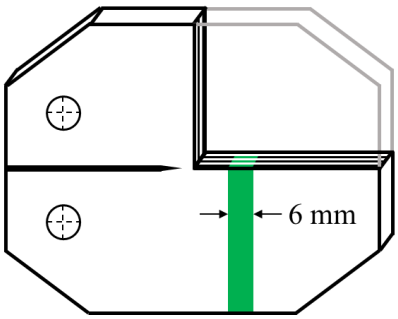

Figure 2: Schematic illustration of a strip sample. Note that the strip was only located in the plies of interest, thus only in the middle 6 0° plies.

Table III: Overview of all the examined lay-up designs with the average thickness and fibre volume fraction of the plies of interest.

Lay-up design	**Thickness plies of interest [µm]**	**V_f plies of interest [%]**
CF ply	358 ± 8	41 ± 4
PAR fibre ply	220 ± 13	49 ± 5
PBO fibre ply	247 ± 11	50 ± 2
Aramid fibre ply	167 ± 21	51 ± 16
PAR fibre strip in CF ply	376 ± 4	/
PBO fibre strip in CF ply	373 ± 4	/
Aramid fibre strip in CF ply	362 ± 8	/

2.3.2 Test and data reduction

The compact tension tests were performed on a universal testing machine equipped with a 30 kN load cell. The crosshead speed was 1.25 mm/min. At least 7 samples of each design strategy were tested. Figure 3 shows a sample in the test set-up. Twisting and

Euler buckling of the samples during testing is a common undesired failure mechanism in compact tension tests. Literature suggests that the use of anti-buckling guides [33, 47, 48] or stiffener plates [49, 50] can prevent this without influencing in-plane compliance [33, 49]. Anti-buckling guides were used at the top and bottom of the samples and worked together with the CF outer layers to prevent buckling and compressive failure. The bolts used to clamp the anti-buckling guides were hand tightened to prevent an influence of the anti-buckling guides on the test measurements by allowing the anti-buckling guides to freely rotate in the vertical plane. Any potential influence of the anti-buckling guides on the test measurements was checked in the past by interrupting a test to remove the anti-buckling guides [36]. No change in the load was observed after removal, confirming that the guides did not affect the test result.

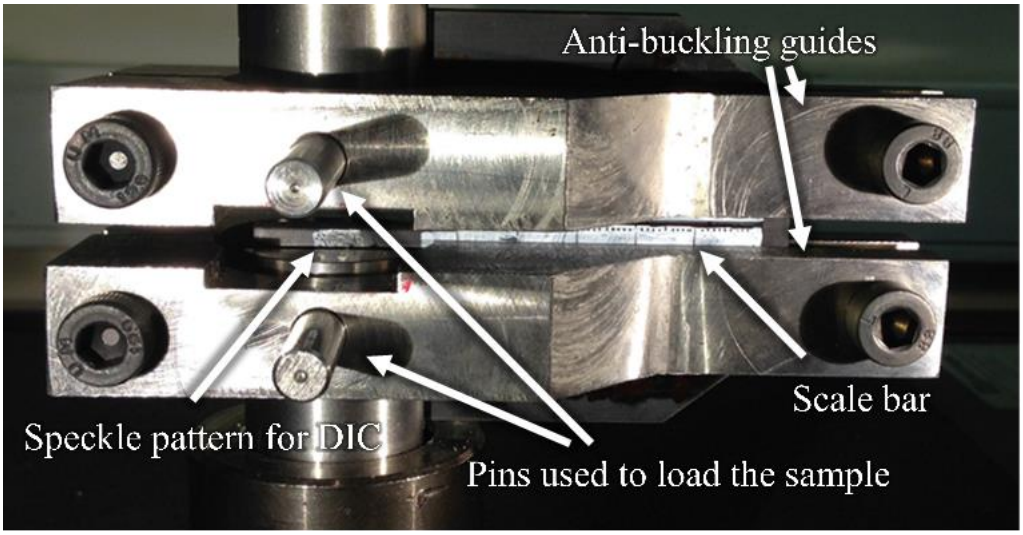

Figure 3: Example of a compact tension test sample in the test set-up.

A camera setup with a resolution of 1392 x 1040 pixels took 2 images per second from one side of the samples during testing. A scale bar with millimetre increments on the samples aided the visual measurement of the crack tip position. At the load points, a speckle pattern was used to follow the opening of the specimen using digital image correlation. Vic-2D 2009 of Correlated Solutions was used to perform the digital image correlation.

The compliance calibration technique was used to process the compact tension test data, see equation 3. The translaminar fracture toughness is described by the critical strain energy release rate G_{Ic}. P_c is the critical load at which crack propagation occurs, t is the material thickness and dC/da is the derivative of the compliance C with respect to the crack length a.

$$G_{Ic} = \frac{P_c^2}{2t}\frac{dC}{da} \tag{3}$$

A finite element model was used to obtain the theoretical compliance of the samples as a function of the crack length. The experimental compliance was used to scale the theoretical compliance and check whether the scaled theoretical compliance matched the experimental compliance. Using the theoretical compliance had three main advantages.

- To obtain the experimental compliance over the entire possible crack length range in small increments, a sample of each design would have to be tested with a range of known crack lengths.
- Using the obtained compliance as a function of the crack length would not account for variations between the individual samples.
- The experimental compliance as a function of crack length is not perfectly smooth. This leads to complications when taking the derivative of the compliance with respect to the crack length in the data reduction.

The Abaqus 2018 finite element model used the same geometry and lay-up designs as the samples used during testing. Only one half of a sample was modelled due to symmetry. The model was based on 10833 quadratic quadrilateral S8R and quadratic triangle STRI65 shell elements with a local mesh refinement down to element sizes of 0.2 mm. A 10 N load was applied at the loading points to calculate the theoretical compliance at a given crack length. This calculation was repeated for all possible crack

lengths in 1 mm increments. Table IV displays the engineering constants of the unidirectional plies that were used in the finite element model for compliance calibration.

Table IV: Engineering constants of the unidirectional plies that were used in the finite element model for compliance calibration. These were calculated from the fibre and matrix properties or estimated from the literature [51, 52].

	E_{11} [GPa]	E_{22} [GPa]	G_{12} [GPa]	G_{23} [GPa]	ν_{12} [/]
CF/epoxy	90.2	3.26	1.27	1.24	0.35
PAR fibre/epoxy	39.3	0.97	1.25	0.90	0.35
PBO fibre/epoxy	136.8	2.60	1.26	0.80	0.35
Aramid fibre/epoxy	56.8	2.59	1.28	1.24	0.43

To prevent a mismatch between the theoretical compliance and the experimental compliance due to specimen-to-specimen variability and difficult-to-avoid errors in model parameters, the theoretical compliance was scaled to fit the experimental compliance. The scaling factor was calculated for each individual sample by matching the theoretical and the experimental compliance in the only point where the experimental crack length is precisely known. This is at the initial crack length, thus at the very beginning of the compact tension test. This initial crack length was measured using a ruler with 0.5 mm increments.

Figure 4 displays an example of this scaling step. A discrepancy exists between the original theoretical compliance data and the experimental compliance of the sample. In contrast, the scaled theoretical compliance data corresponds well with the experimental compliance of the sample.

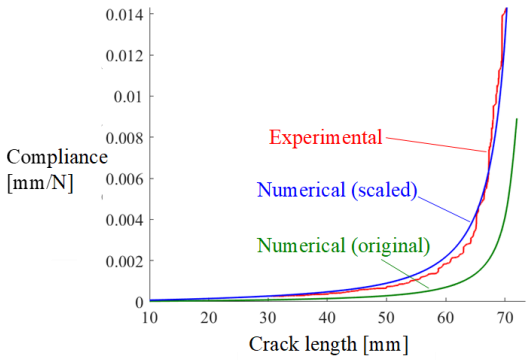

Figure 4: Example of scaling the numerical compliance as a function of the crack length to fit the experimental data.

In the R-curves, the initiation toughness was calculated as G_{Ic} at a crack extension of 0 mm. The initiation zone length was determined as the crack length at which the initiation zone ends and therefore the propagation zone starts. The propagation toughness was calculated as the average of all the data points in the propagation region.

2.3.3 Fractography

Scanning electron microscopy (SEM) was performed using a Philips XL 30 FEG SEM to investigate the fracture surface. The samples were coated with a 5 nm thick platinum layer to avoid charging effects. Secondary electrons were used to perform the SEM analysis. The pictures were taken by tilting the samples under an angle of 20° perpendicular to the fracture plane. An electron acceleration voltage of 5 keV or 10 keV was found to give the best results.

2.3.4 X-ray computed tomography

X-ray computed tomography (XCT) was performed on a PAR fibre ply sample to obtain a better understanding of the behaviour of the composites during compact tension testing. Figure 5 shows the ex-situ compact tension test set-up that was developed for this purpose. The setup was designed to be as small as possible to minimise the source-to-specimen distance while being capable to withstand the forces required for crack growth in the specimen. A specimen could be inserted with perfect perpendicular alignment, using the four adjustment screws. Crack growth was realised by moving the loading pins apart, similar to performing a compact tension test in a universal testing

machine. This displacement of the loading pins was achieved by manually rotating the translation screw using a double-end adjustable tap wrench. The centre line of the specimen stayed aligned in the middle of the setup due to the design of the translation screw. The translation screw changed thread direction in the middle so both loading pins moved in an equidistant but opposite direction. A groove in the middle of the translation screw was used combined with a pin in the setup to keep the middle of the screw in the middle of the setup. This way, the volume of interest stayed aligned with the vertical axis of rotation during scanning. Only height adjustments in between crack growth steps were required because the volume of interest moved downward as the geometry of the specimen changed due to the loading points moving apart.

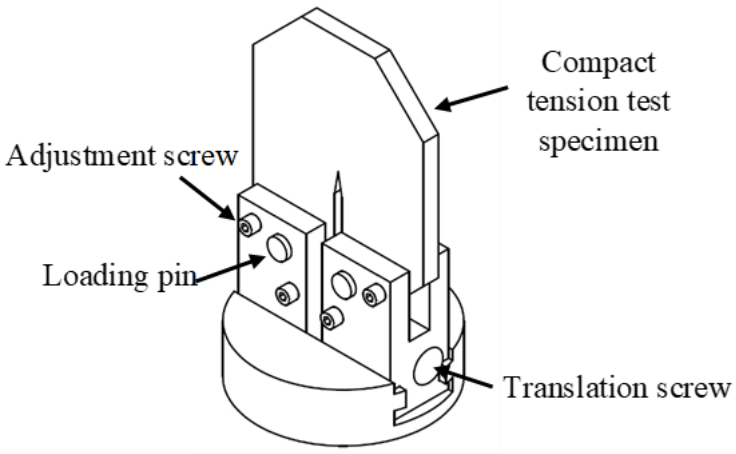

Figure 5: Illustration of the ex-situ XCT compact tension test set-up.

The ex-situ XCT of the PAR fibre ply sample was performed in a microfocus TESCAN UniTOM XL. The UniTOM XL had an open type reflection 230kV/300W X-ray tube source. The detector had a field-of-view of 2856x2856 pixels with a 150 µm pixel pitch. Both the source-to-specimen distance and source-to-detector distance could be adjusted to obtain the desired magnification to optimally image the volume of interest. A full overview of the scan settings is shown in Table V.

Table V: The scan settings used to perform the XCT of the PAR fibre ply sample.

Acceleration voltage source	[kV]	110
Target power	[W]	15

Exposure time	[ms]	505
Nr. of averages	[/]	2
Projections per 360°	[/]	3500
Source-to-object distance	[mm]	60
Source-to-detector distance	[mm]	1500
Magnification	[/]	25x
Voxel size	[µm]	6
Hardware filter	[/]	/

Reconstruction of the sectional planes was performed in the TESCAN Panthera reconstruction and visualization software. The 3D renderings with isotropic voxels were generated in Avizo 3D 2021.1. Avizo 3D 2021.1 was also used to visualise the 2D slices.

3. Results

3.1 Ply samples

Figure 6 shows representative load/displacement graphs of the ply samples. The CF ply samples showed few but large load drops, seen as few but large crack increments, indicating unstable crack growth. In contrast, the PAR and PBO fibre ply samples exhibited stable crack growth with many small crack increments and load drops. The aramid fibre ply samples displayed behaviour that was more like the behaviour of the CF ply samples, and unlike the behaviour of the other two HPPF types. The aramid fibre ply samples showed unstable crack growth, although with more and smaller load drops than the CF ply sample.

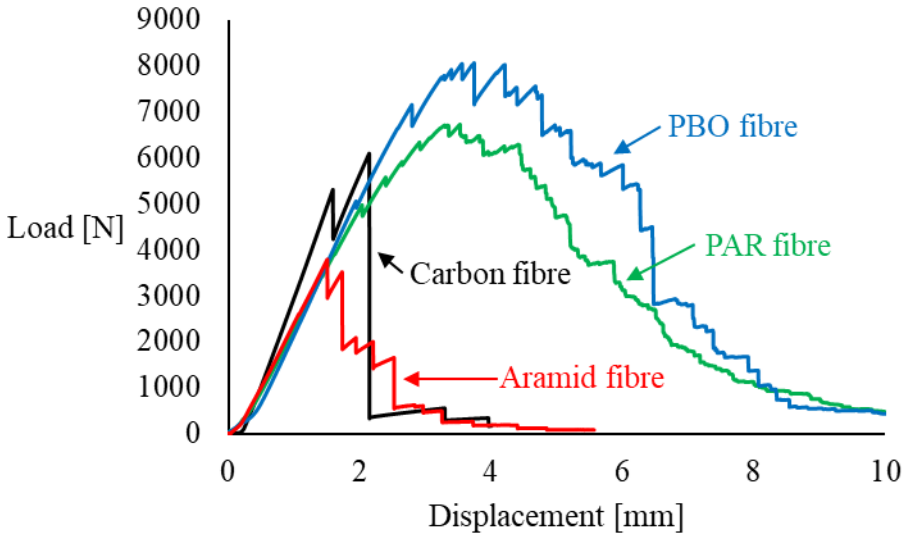

Figure 6: Representative load-displacement curves of the different ply samples.

Figure 7 shows a representative R-curve of a PAR fibre sample. This behaviour is also representative for the PBO fibre samples, see Figure 8a. Two clear regions in the curve can be distinguished. In the initiation zone, when the crack length is still small, the critical strain energy release rate G_{Ic} rises with increasing crack growth as the process zone is still developing. In conventional brittle fibre composites, these energy dissipating mechanisms are mainly fibre debonding and fibre pull-out [28].

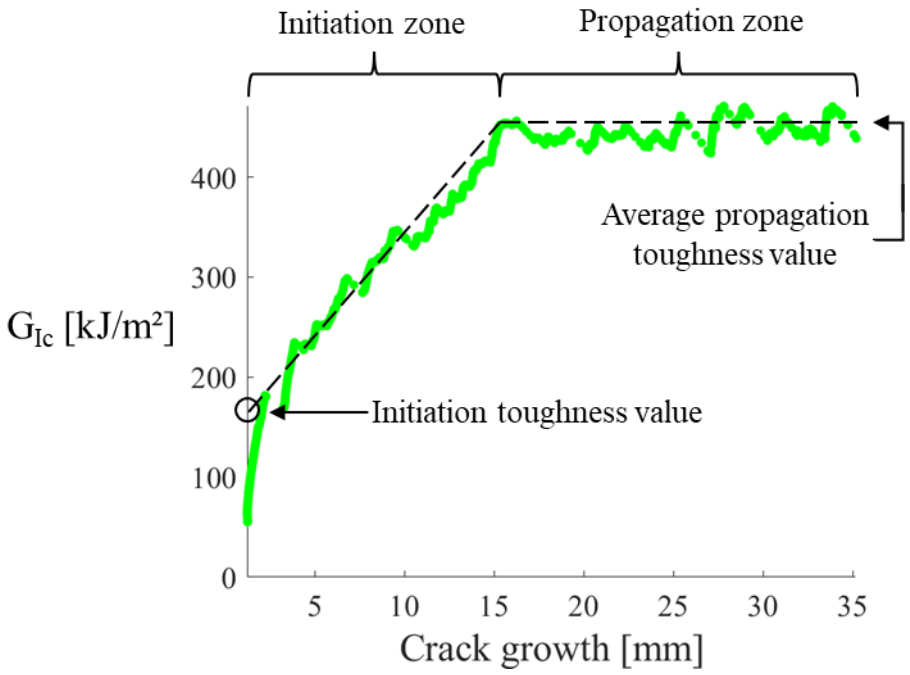

Figure 7: A representative R-curve of a PAR fibre ply sample. A clear transition between the initiation and the propagation zone can be noticed.

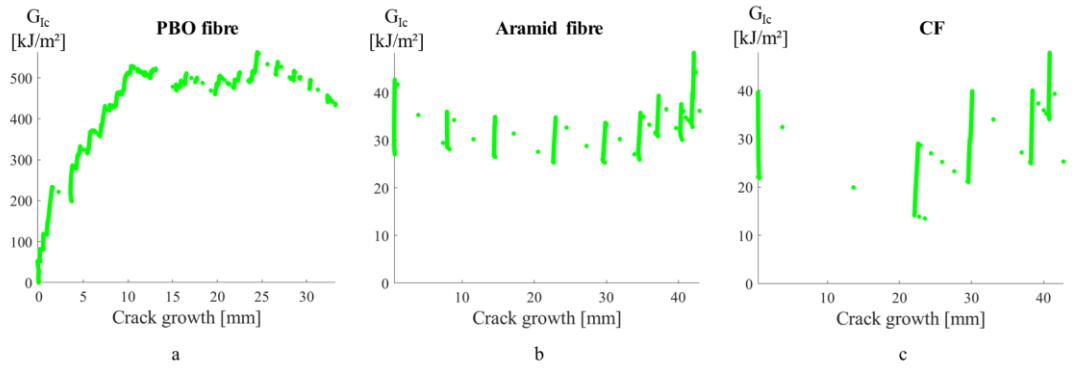

Figure 8: Representative R-curves of the other ply specimens: (a) a PBO fibre ply sample. A clear transition between the initiation and the propagation zone can be noticed, (b) an aramid fibre ply sample. No clear transition between the initiation and the propagation zone can be noticed. Therefore, the initiation toughness value is not reported for the aramid fibre ply samples, and (c) a CF ply sample. No clear transition between the initiation and the propagation zone can be noticed. Therefore, the initiation toughness value is not reported for the CF ply samples.

For the aramid fibre and CF ply samples, no clear R-curve behaviour was observed due to the unstable crack growth, see Figure 8b and Figure 8c. Since there were insufficient data points in the initiation region, no initiation toughness values could be calculated for these design strategies. The obtained values were used to calculate propagation toughness as the values used represent a state in which the process zone is fully developed. Figure 9 presents the measured toughness values of all the ply samples.

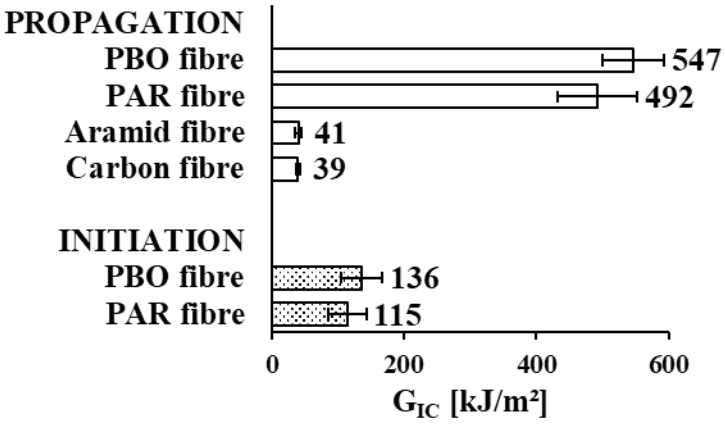

Figure 9: The propagation translaminar fracture toughness values of the ply samples. The initiation translaminar fracture toughness values of the PAR and PBO fibre ply samples are also shown.

3.2 Strip samples

Figure 10 shows a representative load/displacement diagram of a PAR fibre strip sample. This graph is also representative of the behaviour of the PBO fibre strip samples. Initially, the crack had to propagate through CF in the plies of interest before it

reached the strip region. This corresponds to the large load drop in the load/displacement diagram with large crack increment in the sample. However, once the crack tip reached the PAR or PBO fibre strip, the crack growth slowed down significantly. This can be seen in the graph as the smaller load drops between a displacement of 1.5 and 3.2 mm. Moreover, Figure 11 reveals that the strip managed to bridge the crack opening when the crack tip propagated past the strip region. Catastrophic failure occurred when the crack tip grew too far beyond the strip region and the strip could not bridge the crack opening anymore. This crack jump was large enough to grow to the end of the sample, effectively cleaving the sample into two halves.

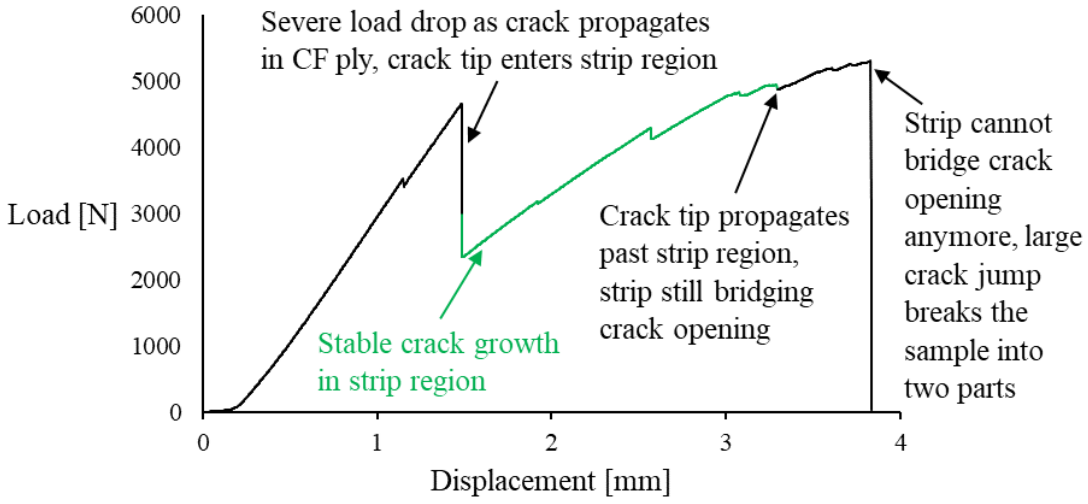

Figure 10: Representative load/displacement diagram of a PAR fibre strip sample. A similar behaviour was noticed with the PBO fibre strip samples.

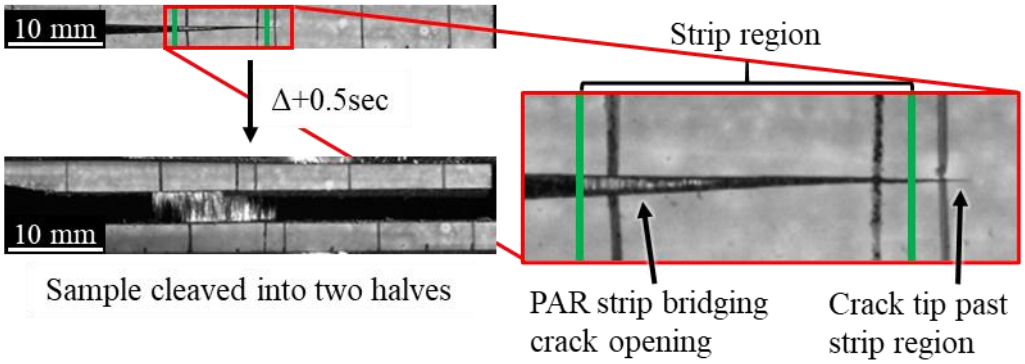

Figure 11: Representative example of a PAR fibre strip bridging the crack opening in a strip sample. The images correspond to the load/displacement diagram at a displacement of ± 3.8 mm, just before and after failure. The strip was able to arrest crack growth even after the crack tip propagated past the strip region. As the strip was not able to carry the load anymore when the crack tip progressed too far beyond the strip region, a large crack jump occurred that effectively split the sample into two halves.

Figure 12a displays a representative R-curve for the PAR fibre strip sample. The PBO fibre strip samples showed a similar behaviour, as is demonstrated in Figure 12b. A clear increase in G_{Ic} is noticed once the crack tip propagates into the strip region. The R-curve still showed an increasing trend as the crack grew at the end of the strip region. This indicates that the full potential of the strip to locally reinforce the material has not been reached. Therefore, and due to the spreading and moving of the strips in the samples during production, the toughness values of the strip samples cannot be quantified. The abrupt failure of the sample when the strip could not carry the load anymore is displayed by a lack of datapoints for larger crack growths.

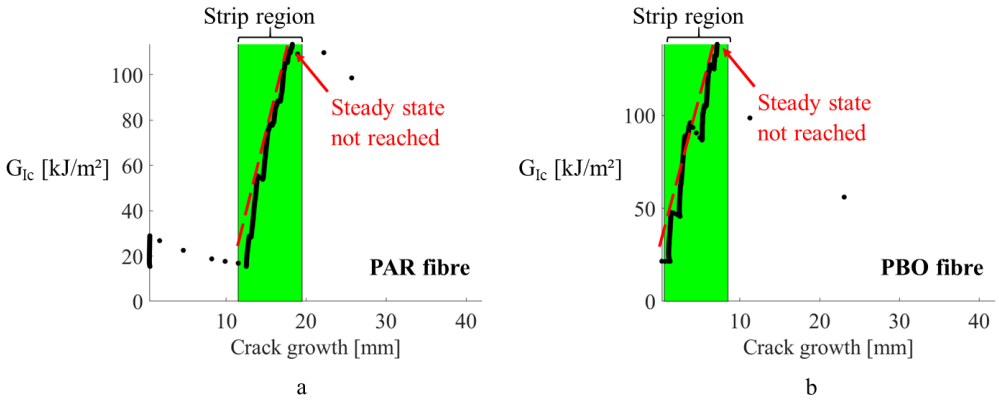

Figure 12: Representative R-curves of (a) a PAR fibre strip sample and (b) a PBO fibre strip sample. A clear increase in toughness can be observed as the crack tip enters the strip region.

No results are shown of the aramid strip sample as no clear improvements over the CF reference were noticed.

3.3 Fractography

A clear difference in the fracture surfaces of the different fibre types was noticed, see Figure 13. The fracture surface of the CF composites indicated brittle fibre failure with short pull-out lengths, up to 0.3 mm. In contrast, the HPPFs revealed a more fuzzy appearance of the fibres with longer pull-out lengths, up to 10 mm for PAR fibres. This appearance is typical for the fibrillation of the high-performance polymer fibres (see Figure 14).

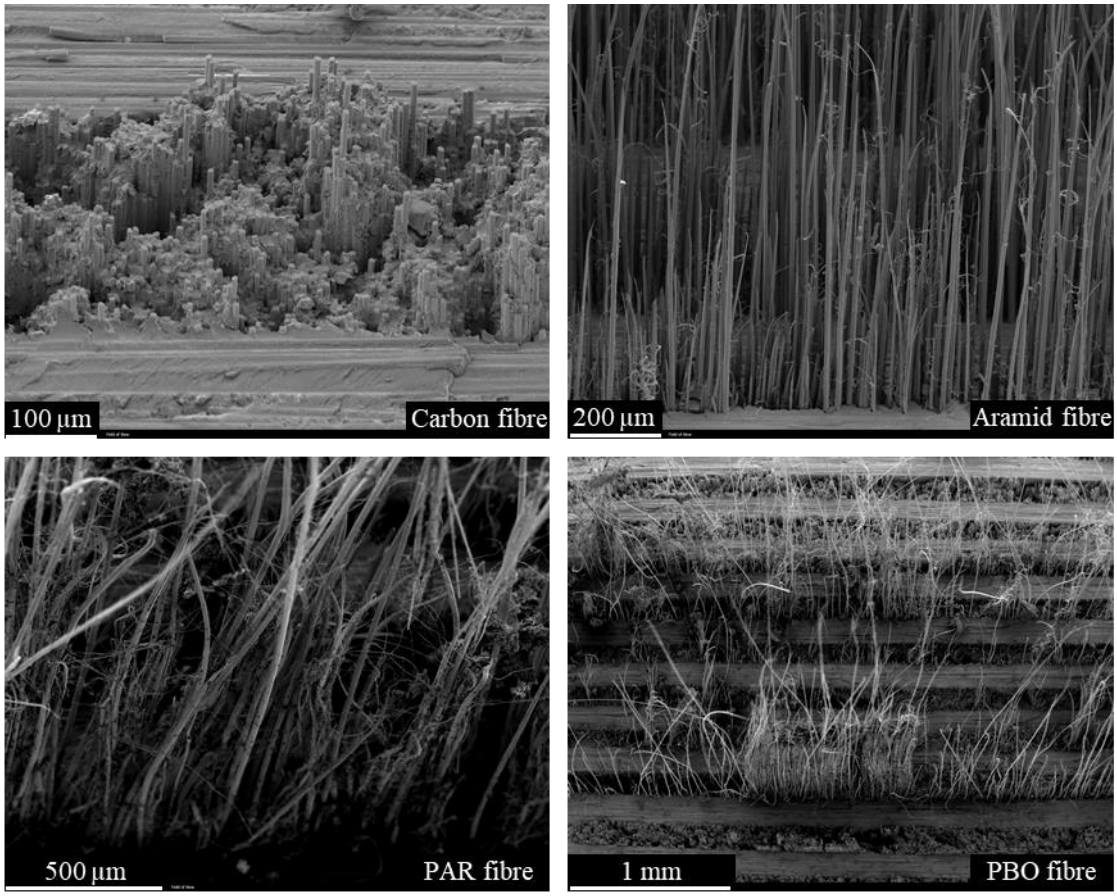

Figure 13: Examples of the fracture surface of the ply specimen of the different fibre types. Short pull-out length can be seen in the CF sample while longer pull-out lengths are noticed in the HPPF samples.

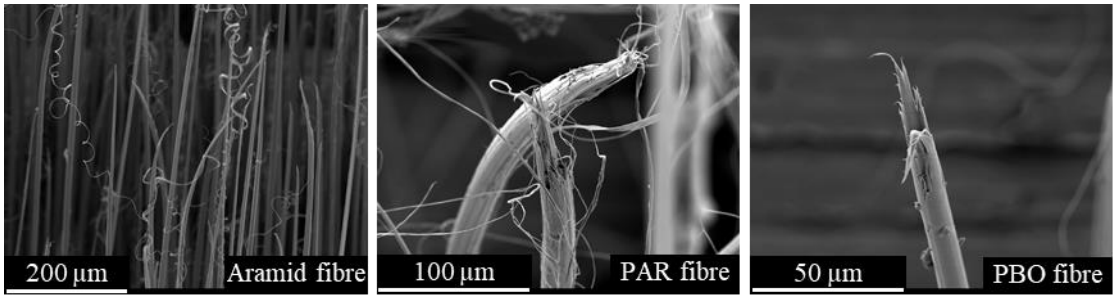

Figure 14: Example of the fibrillation observed in the different HPPF types.

Figure 15 reveals a difference in failure behaviour between the high-performance polymer fibre samples. Whereas the aramid and PAR fibres failed independently from each other, the PBO fibres tended to form clusters.

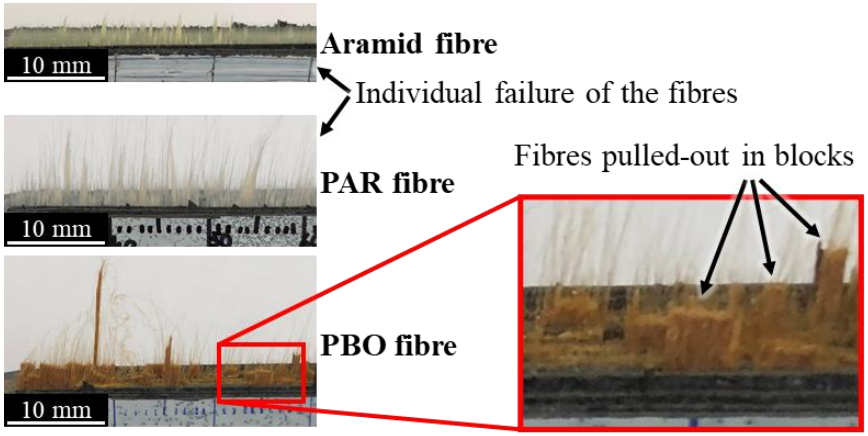

Figure 15: Difference in failure behaviour of the high-performance polymer fibres. Whereas the aramid and PAR fibres failed more in an individual way, some clustering/blocking behaviour can be seen with the PBO fibres.

The PAR and PBO fibre samples displayed a remarkable fracture surface, see Figure 16. The fibre pull-out lengths depended on the ply location. The two outer high-performance polymer fibres plies showed longer pull-out lengths, while the inner plies showed significantly shorter pull-out lengths. This behaviour was likely caused by delaminations between the 90° CF ply and the outer 0° HPPF ply, as will be shown in section 3.4. The aramid fibre samples did not show this behaviour.

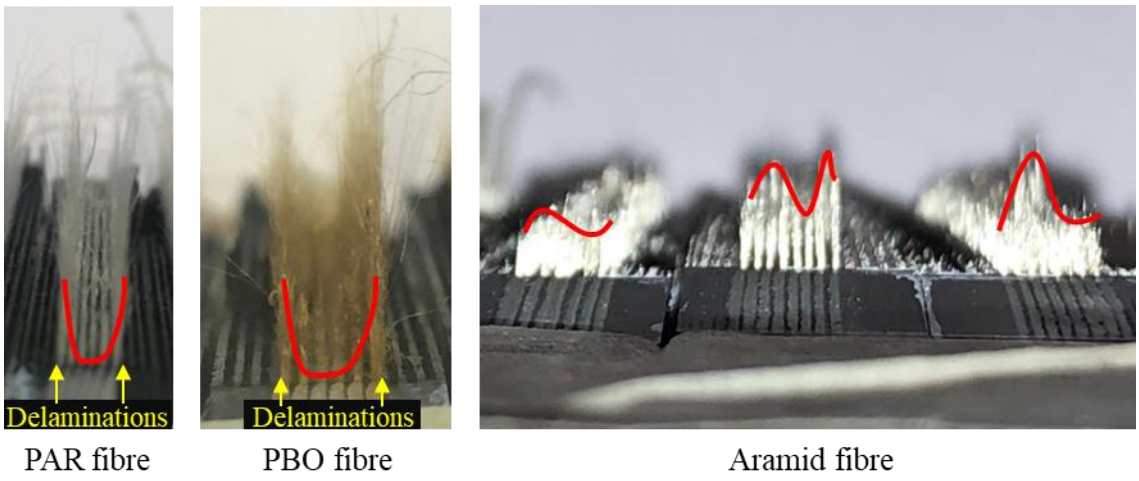

Figure 16: Longer pull-out lengths in the outer plies-of-interest noticed in the PAR and PBO fibre samples. The aramid sample did not show this behaviour as the pull-out lengths of the different aramid plies varied from sample to sample.

3.4 X-ray computed tomography

The XCT pictures provided a better understanding of the failure behaviour of the PAR fibre ply specimens during testing. Figure 17 shows delaminations between the outer 0° PAR fibre plies and the neighbouring 90° CF plies. In the region inside the plies-of-

interest, no damage is visible yet, while a crack can be noticed in the outer 0°/90° CF plies. As crack opening displacement continues, the inner 0° PAR fibre plies fail closer to the fracture plane while the outer 0° PAR fibre plies fail further away from the fracture plane, see Figure 18. This investigation supports the observation made in Figure 16.

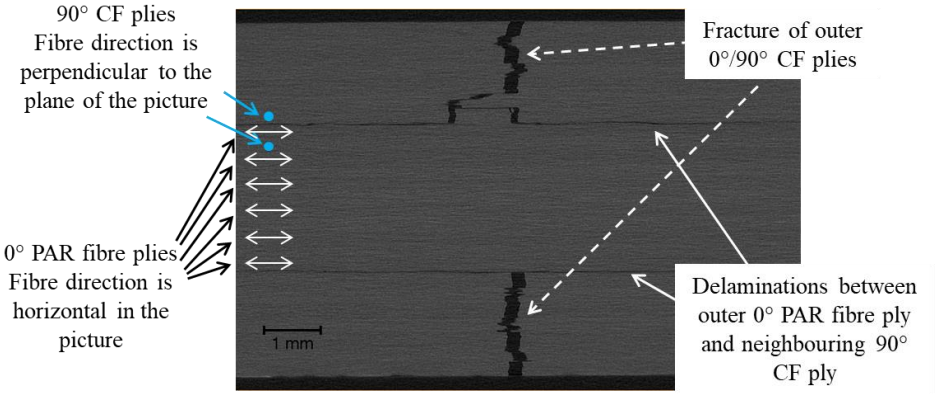

Figure 17: XCT picture of a PAR fibre ply specimen. Delaminations between the outer 0° PAR fibre plies and the neighbouring 90° CF plies can be observed.

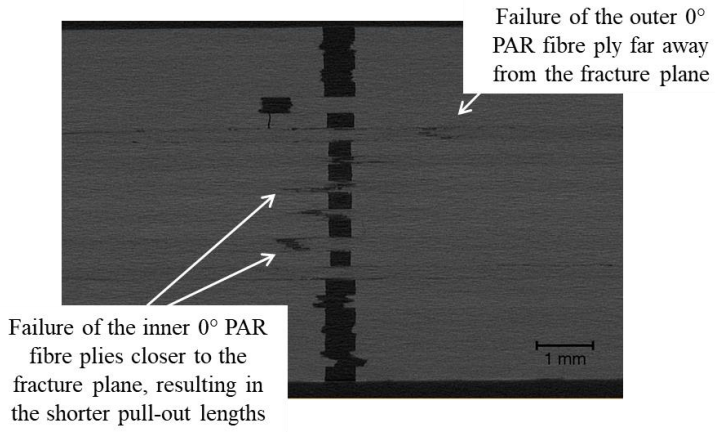

Figure 18: XCT picture of the PAR fibre ply specimen at a larger crack opening displacement. Failure of the inner 0° PAR fibre plies fail closer to the fracture plane while the outer 0° PAR fibre plies fail further away from the fracture plane can be noticed.

4. Discussion

4.1 Ply samples

The CF ply samples displayed unstable crack growth with few but large crack increments. The calculated average propagation toughness of 39 kJ/m² was relatively low given the average ply thickness of 358 µm [53]. However, it is important to note that the fibre volume fraction was only 41%, which is quite low for a UD ply [28].

The calculated average propagation toughness of 492 kJ/m² for the PAR fibre ply samples was very high given the average ply thickness of 220 µm with a fibre volume fraction of 49% [28]. The PBO fibre ply samples also exhibited stable crack growth with many very small crack increments. The calculated average propagation toughness of 547 kJ/m² is very high for a composite with an average ply thickness of 247 µm and a fibre volume fraction of 50% [28]. The propagation toughness of 492 kJ/m² for the PAR fibre ply samples and 547 kJ/m² for the PBO fibre ply samples are, to the authors' knowledge, the highest recorded values for the translaminar fracture toughness in the literature. For both the PAR and PBO fibre samples, the very high recorded values cannot be attributed to just the main energy dissipating mechanisms found in conventional, brittle fibre composites, which are fibre debonding and fibre pull-out. It is assumed that the fibrillation of the fibres also was an important energy dissipating mechanism. However, currently no exact values of the contribution of fibrillation towards the overall measured toughness could be extracted.

Besides the energy directly dissipated by fibre fibrillation due to the creation of new surface area between the fibrils, the change in structure of the fibres will also have an influence on the other energy dissipating mechanisms. As the structure of the fibre drastically changes during fibrillation, the energy being dissipated by fibre debonding and especially fibre pull-out is affected. In combination with possible Poisson contractions, the normal force between the fibre and the matrix is affected, which consecutively influences the energy dissipation by friction during fibre pull-out. Moreover, the very long pull-out lengths experienced with the HPPFs can be a consequence of their fibrillation. More research is needed to better understand the failure behaviour of high-performance polymer fibres and its influence on fibre debonding and fibre pull-out.

Not only was there a direct energy dissipation of the high-performance polymer fibres due to the debonding, pull-out and fibrillation of the fibres, an influence on the stress state is also expected. The very long pull-out lengths effectively blunted the crack tip by spreading the crack over a larger area. The fractography investigation reveals a degree of notch insensitivity as many of the fibres had failed far away from the failure plane, see Figure 13 and Figure 15.

While high translaminar toughness values were recorded for the PAR and PBO fibre samples, the results measured for the aramid fibre ply samples were lacklustre. Although a slightly more stable crack growth of the aramid fibre samples over the CF reference was noticed, no significant improvement in translaminar fracture toughness over the CF reference was recorded. Pinpointing an exact cause of the considerably worse performance of the aramid fibre samples compared to the PAR and PBO fibres samples is difficult.

A few possible explanations for this discrepancy were investigated. The ply thickness was lower than the ply thicknesses of PAR and PBO fibre samples, but not to such a degree to be able to explain this difference. Also, no clear origin for the lacklustre performance of the aramid fibre samples could be deduced based on the mechanical properties of all the high-performance polymer fibres in Table I. The aramid fibre property values lay in between those of the PBO and PAR fibres. Another possible explanation was a difference in the fibre/matrix interface. A poor adhesion between the fibres and the matrix will influence the fibre debonding and pull-out. Microdroplet tests have been performed by Schuurbiers et al. to examine interfacial shear strength [54]. However, the interfacial shear strength of aramid/epoxy was similar to PAR/epoxy. Therefore, it is unlikely that a difference in adhesion between aramid/epoxy and PAR/epoxy is the cause of the difference in toughness measured.

Another possible explanation for this difference in performance is the actual composition of the fibres itself. The energy dissipated during fibrillation by the creation of new surface area is dependent on two parameters; the area of new surface created and its surface energy. Potentially the value of one or both parameters is significantly lower for the aramid fibres compared to the PAR and PBO fibres. However, given the challenges related to quantifying the amount of new surface area created upon fibrillation, this currently remains only a hypothesis. This difficulty was already showcased by Syed Abdullah et al. [25]. More research is needed to examine this possible explanation.

4.2 Strip samples

A clear crack arresting capability was noticed in the PAR and PBO fibre strip samples. The strips were able to locally increase the translaminar fracture toughness significantly. Moreover, the strip was able to slow down crack growth by bridging the crack opening even after the crack tip grew beyond the strip region. The strip was not able to bridge the crack opening anymore when the crack tip progressed too far past the strip region. As the CF composite after the strip region had a significantly lower translaminar fracture toughness compared to the strip material, and the load was no longer supported by the strip material, a significant and unstable crack jump occurred. This crack increment consistently grew towards the very end of the sample, thus growing through the remaining length of CF composite after the strip region, effectively cleaving the samples into two halves. However, the full potential to locally reinforce the composite was not reached by the 6 mm wide strip. The R-curve in the strip region still showed an upwards trend towards the end of the strip, indicating it was still in the initiation zone. This finding is supported by the behaviour of the ply samples, where the initiation zone length was 11.6 ± 3.1 mm for the PAR fibre samples, and 13.5 ± 3.1 mm for the PBO

fibre samples. Therefore, to reach the full potential of the strips, a width of at least 11.6 and 13.5 mm is recommended when using PAR and PBO strips, respectively.

Although the PAR and PBO fibre strips showed a crack arresting capability in CF plies, the aramid fibre strip samples did not. No significant improvements of the CF reference samples were noticed. This behaviour can be linked to the lacklustre performance of the aramid fibre ply samples in translaminar fracture.

5. Conclusion

A novel lay-up design of compact tension specimens was used to successfully characterise the translaminar fracture toughness of HPPF composites. The PAR and PBO fibre ply composites showed a very stable crack growth. The propagation toughness of the two HPPFs are among the highest recorded values for the translaminar fracture toughness in the literature. This demonstrates the potential of partially replacing CFs with HPPFs to obtain composites with an improved translaminar fracture toughness. Substantial fibrillation of the fibres was observed, alongside long pull-out lengths. While typical CF pull-out lengths can be in the 0.3 mm range, pull-outs in the 10 mm range were recorded for the PAR fibres. The long pull-outs do not only contribute directly to energy dissipation during crack growth, but also effectively blunt the crack tip.

The PAR and PBO fibre strips showed great potential to locally reinforce the material. The strips were able to arrest the crack growth significantly and were even able to bridge the crack opening after the crack tip progressed beyond the strip region. A strip width of at least 11.6 mm when using PAR fibres or 13.5 mm when using PBO fibres is advised to reach the full potential of the fibres to locally reinforce a composite laminate.

The aramid fibre composite showed lacklustre performance. No clear origin why exactly the aramid fibre composites performed so poorly compared to the two other

high-performance polymer fibre composites could be assigned. However, it was hypothesized that the explanation can be found in the extent of energy dissipation during the fibrillation of the fibres. Future studies are needed to investigate this hypothesis.

Acknowledgements

The authors gratefully acknowledge SIM and VLAIO for their support of the SBO project RELFICOM, running in the NANOFORCE Program. YS acknowledges FWO Flanders for his postdoctoral fellowship.

References

1. Davies, P., et al., *Round-robin interlaminar fracture testing of carbon-fibre-reinforced epoxy and PEEK composites.* Composites Science and Technology, 1992. **43**(2): p. 129-136.
2. Martin, R.H., *Interlaminar fracture characterization: A current review*, in *2nd Japan International SAMPE Symposium*. 1991, NASA: Tokyo, Japan.
3. O'Brien, T.K., *Interlaminar fracture toughness: the long and winding road to standardization.* Composites Part B: Engineering, 1998. **29**(1): p. 57-62.
4. Sela, N. and O. Ishai, *Interlaminar fracture toughness and toughening of laminated composite materials: a review.* Composites, 1989. **20**(5): p. 423-435.
5. Tanaka, K., K. Kageyama, and M. Hojo, *Prestandardization study on mode II interlaminar fracture toughness test for cfrp in japan.* Composites, 1995. **26**(4): p. 257-267.
6. Gutkin, R., et al., *Modelling the R-curve effect and its specimen-dependence.* International Journal of Solids and Structures, 2011. **48**(11–12): p. 1767-1777.
7. Pinho, S.T., P. Robinson, and L. Iannucci, *Developing a four point bend specimen to measure the mode I intralaminar fracture toughness of unidirectional laminated composites.* Composites Science and Technology, 2009. **69**(7–8): p. 1303-1309.
8. Jacobsen, T.K. and B.F. Sørensen, *Mode I intra-laminar crack growth in composites — modelling of R-curves from measured bridging laws.* Composites Part A: Applied Science and Manufacturing, 2001. **32**(1): p. 1-11.
9. Wells, J.K. and P.W.R. Beaumont, *Debonding and pull-out processes in fibrous composites.* Journal of Materials Science, 1985. **20**(4): p. 1275-1284.
10. Bullegas, G., S.T. Pinho, and S. Pimenta, *Engineering the translaminar fracture behaviour of thin-ply composites.* Composites Science and Technology, 2016. **131**: p. 110-122.
11. Teixeira, R., S.T. Pinho, and P. Robinson, *Translaminar ply fracture toughness of advanced composites*, in *18th International Conference on Composite Materials*. 2011: Jeju Island, South Korea.
12. Catalanotti, G., et al., *Measurement of resistance curves in the longitudinal failure of composites using digital image correlation.* Composites Science and Technology, 2010. **70**(13): p. 1986-1993.

13. Laffan, M.J., et al., *Translaminar fracture toughness: The critical notch tip radius of 0° plies in CFRP.* Composites Science and Technology, 2011. **72**(1): p. 97-102.
14. Marín, L., et al., *Hygrothermal effects on the translaminar fracture toughness of cross-ply carbon/epoxy laminates: Failure mechanisms.* Composites Science and Technology, 2016. **122**: p. 130-139.
15. Gao, Y.-C., Y.-W. Mai, and B. Cotterell, *Fracture of fiber-reinforced materials.* Zeitschrift für angewandte Mathematik und Physik ZAMP, 1988. **39**(4): p. 550-572.
16. Kim, J.-K. and Y.-w. Mai, *High strength, high fracture toughness fibre composites with interface control—A review.* Composites Science and Technology, 1991. **41**(4): p. 333-378.
17. Fila, M., C. Bredin, and M.R. Piggott, *Work of fracture of fibre-reinforced polymers.* Journal of Materials Science, 1972. **7**(9): p. 983-988.
18. Kelly, A., *Interface Effects and the Work of Fracture of a Fibrous Composite.* Proceedings of the Royal Society of London. A. Mathematical and Physical Sciences, 1970. **319**(1536): p. 95-116.
19. Naito, K., *Tensile properties and weibull modulus of some high-performance polymeric fibers.* Journal of Applied Polymer Science, 2013. **128**(2): p. 1185-1192.
20. Hunsaker, M.E., G.E. Price, and S.J. Bai, *Processing, structure and mechanics of fibres of heteroaromatic oxazole polymers.* Polymer, 1992. **33**(10): p. 2128-2135.
21. Krause, S.J., et al., *Morphology and properties of rigid-rod poly(p-phenylene benzobisoxazole) (PBO) and stiff-chain poly(2,5(6)-benzoxazole) (ABPBO) fibres.* Polymer, 1988. **29**(8): p. 1354-1364.
22. Hu, X.-D., et al., *Rigid-Rod Polymers: Synthesis, Processing, Simulation, Structure, and Properties.* Macromolecular Materials and Engineering, 2003. **288**(11): p. 823-843.
23. Herráez, M., et al., *Strength and toughness of structural fibres for composite material reinforcement.* Philosophical transactions. Series A, Mathematical, physical, and engineering sciences, 2016. **374**(2071): p. 20150274-20150274.
24. Honjo, K., *Fracture toughness of PAN-based carbon fibers estimated from strength–mirror size relation.* Carbon, 2003. **41**(5): p. 979-984.
25. Abdullah, S.I.B.S., L. Iannucci, and E.S. Greenhalgh, *On the translaminar fracture toughness of Vectran/epoxy composite material.* Composite Structures, 2018. **202**: p. 566-577.
26. Laffan, M.J., et al., *Translaminar fracture toughness testing of composites: A review.* Polymer Testing, 2012. **31**(3): p. 481-489.
27. Teixeira, R.F., S.T. Pinho, and P. Robinson, *Thickness-dependence of the translaminar fracture toughness: Experimental study using thin-ply composites.* Composites Part A: Applied Science and Manufacturing, 2016. **90**: p. 33-44.
28. Pimenta, S. and S.T. Pinho, *An analytical model for the translaminar fracture toughness of fibre composites with stochastic quasi-fractal fracture surfaces.* Journal of the Mechanics and Physics of Solids, 2014. **66**: p. 78-102.
29. Catalanotti, G., et al., *Determination of the mode I crack resistance curve of polymer composites using the size-effect law.* Engineering Fracture Mechanics, 2014. **118**: p. 49-65.
30. Kolednik, O., et al., *Bioinspired Design Criteria for Damage-Resistant Materials with Periodically Varying Microstructure.* Advanced Functional Materials, 2011. **21**(19): p. 3634-3641.
31. Sistaninia, M. and O. Kolednik, *Effect of a single soft interlayer on the crack driving force.* Engineering Fracture Mechanics, 2014. **130**: p. 21-41.

32. Sistaninia, M. and O. Kolednik, *Improving strength and toughness of materials by utilizing spatial variations of the yield stress.* Acta Materialia, 2017. **122**: p. 207-219.
33. Swolfs, Y. and S.T. Pinho, *3D printed continuous fibre-reinforced composites: Bio-inspired microstructures for improving the translaminar fracture toughness.* Composites Science and Technology, 2019. **182**: p. 107731.
34. Arun, K.V., R. Kamat, and S. Basavarajappa, *Mechanism of Translaminar Fracture in Glass/Textile Fabric Polymer Hybrid Composites.* Journal of Reinforced Plastics and Composites, 2010. **29**: p. 254-265.
35. Munro, M. and C.P.Z. Lai, *The elevated-temperature dependence of fracture energy mechanisms of hybrid carbon-glass fibre reinforced composites.* Journal of Materials Science, 1988. **23**(9): p. 3129-3136.
36. Swolfs, Y., et al., *The importance of translaminar fracture toughness for the penetration impact behaviour of woven carbon/glass hybrid composites.* Composites Part A: Applied Science and Manufacturing, 2017. **103**: p. 1-8.
37. Amacher, R., et al., *Toward aerospace grade thin-ply composites*, in *ECCM17 - 17th European Conference on Composite Materials*. 2016: Munich, Germany.
38. Cugnoni, J., et al., *Translaminar fracture of regular and hybrid thin ply composites: experimental characterization and modeling*, in *ECCM18*. 2018: Athens, Greece.
39. Katafiasz, T.J., L. Iannucci, and E.S. Greenhalgh, *Development of a novel compact tension specimen to mitigate premature compression and buckling failure modes within fibre hybrid epoxy composites.* Composite Structures, 2019. **207**: p. 93-107.
40. Breite, C., et al., *Aligning Fibre Break Models for Composites with the Observable Micro-Scale Material Behaviour*. 2021, KU Leuven: Leuven.
41. Blanco, N., et al., *Intralaminar fracture toughness characterisation of woven composite laminates. Part I: Design and analysis of a compact tension (CT) specimen.* Engineering Fracture Mechanics, 2014. **131**: p. 349-360.
42. Wang, D.H., H. Jiang, and W. Wade Adams, *Rigid-Rod Polymers*, in *Encyclopedia of Polymer Science and Technology*. 2011.
43. Teixeira, R., *Translaminar fracture toughness of CFRP: from the toughness of individual plies to the toughness of the laminate*, in *Department of Aeronautics*. 2015, Imperial College London. p. 197.
44. Pinho, S.T., P. Robinson, and L. Iannucci, *Fracture toughness of the tensile and compressive fibre failure modes in laminated composites.* Composites Science and Technology, 2006. **66**(13): p. 2069-2079.
45. Laffan, M.J., et al., *Measurement of the in situ ply fracture toughness associated with mode I fibre tensile failure in FRP. Part II: Size and lay-up effects.* Composites Science and Technology, 2010. **70**(4): p. 614-621.
46. Ortega, A., et al., *Translaminar fracture toughness of interply hybrid laminates under tensile and compressive loads.* Composites Science and Technology, 2017. **143**: p. 1-12.
47. Harris, C.E. and D.H. Morris, *Fracture behavior of thick, laminated graphite/epoxy composites*. 1984, Virginia Polytechnic Institute. p. 189.
48. Kongshavn, I. and A. Poursartip, *Experimental investigation of a strain-softening approach to predicting failure in notched fibre-reinforced composite laminates.* Composites Science and Technology, 1999. **59**(1): p. 29-40.
49. Slepetz, J.M. and L. Carlson, *Fracture of Composite Compact Tension Specimens.* ASTM Special Technical Publication 593, 1976: p. 143 - 162.
50. Poe, C.C. and J.R. Reeder, *Fracture behavior of a stitched warp-knit carbon fabric composite*, NASA, Editor. 2001, NASA: Langley research center, Hampton, Virginia.

51. Huang, Y.K., P.H. Frings, and E. Hennes, *Mechanical properties of Zylon/epoxy composite*. Vol. 33. 2002, Kidlington, Royame-Uni: Elsevier.
52. Pindera, M.-J., et al., *Mechanical Response of Aramid/Epoxy under Tensile, Compressive and Shear Loading.* Journal of Reinforced Plastics and Composites, 1989. **8**(4): p. 410-420.
53. Furtado, C., et al., *Is there a ply thickness effect on the mode I intralaminar fracture toughness of composite laminates?* Theoretical and Applied Fracture Mechanics, 2020. **107**: p. 102473.
54. Schuurbiers, K., L. Gorbatikh, and Y. Swolfs, *The compressive behaviour of high-performance polymer fibre-reinforced composites*. 2017, KU Leuven.